

Dual-energy three compartment breast imaging (3CB) for novel compositional biomarkers to improve detection of malignant lesions

Lambert Leong

University of Hawaii Cancer Center <https://orcid.org/0000-0002-2927-8458>

Sergei Malkov

University of California San Francisco

Karen Drukker

University of Chicago

Bethany Niell

Moffitt Cancer Center and Research Institute

Peter Sadowski

University of Hawaii <https://orcid.org/0000-0002-7354-5461>

Thomas Wolfgruber

University of Hawaii Cancer Center <https://orcid.org/0000-0001-8770-1800>

Heather Greenwood

University of California San Francisco

Bonnie Joe

University of California San Francisco

Karla Kerlikowske

University of California at San Francisco

Maryellen Giger

University of Chicago <https://orcid.org/0000-0001-5482-9728>

John John Shepherd (✉ johnshep@hawaii.edu)

University of Hawaii Cancer Center <https://orcid.org/0000-0003-2280-2541>

Article

Keywords: three compartment breast (3CB), breast imaging, breast cancer, malignancy detection

Posted Date: March 8th, 2021

DOI: <https://doi.org/10.21203/rs.3.rs-292446/v1>

License:  This work is licensed under a Creative Commons Attribution 4.0 International License.

[Read Full License](#)

Version of Record: A version of this preprint was published at Communications Medicine on August 31st, 2021. See the published version at <https://doi.org/10.1038/s43856-021-00024-0>.

Dual-energy three compartment breast imaging (3CB) for novel compositional biomarkers to improve detection of malignant lesions

Lambert Leong^{1,2}, Serghei Malkov³, Karen Drukker⁴, Bethany L. Niell⁵, Peter Sadowski⁶, Thomas Wolfgruber¹, Heather Greenwood⁷, Bonnie Joe⁷, Karla Kerlikowske^{3,8}, Maryellen Giger⁴, John A Shepherd^{1*}

1. Department of Epidemiology and Population Sciences, University of Hawaii Cancer Center, Honolulu, HI 96813
 2. Department Molecular Bioscience and Bioengineering, University of Hawaii at Manoa, Honolulu, HI 96822
 3. Departments Epidemiology and Biostatistics, University of California, San Francisco, San Francisco, CA 94115
 4. Department of Radiology, University of Chicago, Chicago, IL 60637
 5. Department of Diagnostic Imaging and Interventional Radiology, H. Lee Moffitt Cancer Center and Research Institute, Tampa, FL, 33612
 6. Department of Information and Computer Science, University of Hawaii at Manoa, Honolulu, HI 96822
 7. Department of Radiology and Biomedical Imaging, University of California, San Francisco, San Francisco, CA 94115
 8. Department of Medicine, University of California, San Francisco, San Francisco, CA 94115
- (*) Corresponding author

Address correspondence to:

John A. Shepherd, Ph.D.
University of Hawai'i Cancer Center
701 Ilalo Street
Honolulu, Hawai'i 96813.
Email: johnshep@hawaii.edu

1 **ABSTRACT**

2 We explore a compositional breast imaging technique known as three compartment breast (3CB) to improve
3 malignancy detection. The addition of 3CB compositional information to computer-aided detection (CAD) software
4 improved malignancy predictions resulting in an area under the receiver operating characteristic curve (AUC) of
5 0.81 (confidence interval (CI) of 0.74-0.88) on a held-out test set, while CAD software alone achieved an AUC of
6 0.69 (CI 0.60-0.78). We also identified that invasive breast cancers have a unique compositional signature
7 characterized by reduced lipid content and increased water and protein content when compared to surrounding
8 tissues. Clinically, 3CB may potentially provide increased accuracy in predicting malignancy and a feasible avenue
9 to explore compositional breast imaging biomarkers.

10 INTRODUCTION

11 Breast cancer is the leading cause of cancer death among women globally¹. Early detection with screening
12 mammography has a beneficial impact on survival and has been shown to reduce cancer mortality.²⁻⁶ However, the
13 accuracy resulting from breast imaging technologies still has room for improvement. For instance, in the U.S., 71%
14 of biopsies do not result in a breast cancer diagnosis suggesting a modest specificity.^{7,8} Furthermore, breast density
15 affects the accuracy of full field digital mammography (FFDM) since dense tissue can mask tumors, diminishing
16 the sensitivity of mammography by 10-20% compared to women with fatty breasts.⁹ Compared to FFDM, digital
17 breast tomosynthesis (DBT) increases cancer detection rates and decreases recall rates. However, the added benefit
18 of DBT is difficult to quantify and studies have demonstrated that, positive biopsy rates following screening DBT
19 are similar to those following screening FFDM.^{9,10} Also, in a registry study including over 1.5 M screening
20 mammograms from 46 registry sites, it was shown that women with the extremely dense breast tissue had neither
21 reduced recall nor increased cancer detection rates for DBT compared to FFDM.¹¹ Improvements to sensitivity and
22 specificity are needed and could result in an increase in detecting malignancies and reduction of unnecessary, benign
23 biopsies.

24 The fundamental information that a radiologist uses, the attenuation of X-rays from a single exposure, has remained
25 the same since the inception of breast imaging in 1913.¹² Without additional information, mammography provides
26 only relative radiopacity (i.e. tissue density relative to a background of fat) and lesion type, such as mass,
27 asymmetry, or calcifications. Lesion classification is limited to detection of calcifications, which are often benign,
28 as well as the shape and symmetry of high-density breast masses. Thus, lesion classification has limited reliability in
29 predicting an invasive breast cancer. Computer-aided detection (CAD) software attempts to improve the diagnostic
30 accuracy of mammography through the utilization of computer vision and artificial intelligence algorithms to
31 automatically identify anomalies.¹³ Yet, the fundamental information used by CAD is identical to the information
32 radiologists use. While CAD has been shown to be clinically beneficial by some,^{14,15} others have shown that the
33 addition of CAD had no significant improvement to screening sensitivity and specificity.¹⁶ It is likely that the limit

34 of diagnostically relevant information from radiologists and/or CAD has been reached with X-ray based, single-
35 energy mammography, especially in women with dense breasts.

36 Additional diagnostic information can be obtained via contrast-enhanced mammography (CEM). Contrast imaging
37 has demonstrated increased sensitivity to detect cancer due to differential vascularization of cancerous and benign
38 tissue.¹⁷ Invasive breast cancer typically presents as a mass of epithelial cells with a high degree of vascularization.
39 IDC, and often DCIS due to its own vascularization, enhance on contrast imaging methods. However, these
40 techniques still have low specificity because benign lesions also enhance with contrast.¹⁸ Like mammography, the
41 diagnostic information gained with contrast imaging is still based in the lesion morphology and structure of
42 surrounding tissue. Since intravenous contrast can cause adverse effects, CEM is often used as a secondary imaging
43 tool. Therefore, radiologists are often not afforded this information on the initial.

44 Radiomic features and imaging biomarkers based on tissue composition have the potential to address accuracy
45 issues seen with current imaging techniques and technologies. Evidence suggests that the biology and atomic of
46 malignant lesions differ from benign lesions and these differences manifest into macroscopically unique tissue
47 compositions which are measurable with multi-spectral X-ray imaging^{19,20}. First, invasive cancer is highly
48 angiogenic and malignant tumors have been shown to consume lipids to sustain high rates of proliferation.^{21,22} The
49 central to peripheral microvasculature of the lesion differs significantly between normal tissue, fibroadenomas (FA)
50 and different grades of invasive ductal carcinoma (IDC).^{23,24} Second, adipocytes, available at the tumor stromal
51 interface, have demonstrated a pro-tumorigenic role for breast cancer.²⁵ Triple negative cancers utilize and require
52 fatty-acid oxidation (FAO) leached from the surrounding tissues. This has been observed using multispectral
53 mammograms as a decrease in fat composition surrounding triple negative cancers versus receptor positive
54 tumors.²⁶ Third, Cerussi et al.²⁷ found a 20% reduction in lipid, and 50% increase in water, content in invasive breast
55 cancer versus normal breast tissue. A strong positive correlation ($R = 0.98$) between the macroscopic water
56 concentration and the Scarff Bloom-Richardson Score (a histological grading scale ranging from 3 to 9, that
57 accounts for tubule formation, nuclear pleomorphism, and mitosis counts) was also reported.²⁸ Fourth, invasive

58 cancers have significantly lower X-ray attenuation than FAs that also lead to biopsy, suggesting a distinctly different
59 composition between cancerous and benign masses¹⁷.

60 The purpose of this study is to demonstrate that compositional profiles of the breast combined with CAD predictions
61 can improve specificity of breast cancer detection. A dual-energy mammography technique known as 3-
62 Compartment Breast (3CB) imaging was used to obtain the lipid-water-protein (LWP) fractions of the breast on a
63 pixel-by-pixel basis. The 3CB scientific principals and imaging protocols have been previously presented^{19,29} as
64 well as the characteristics of malignant versus benign lesions.^{20,30} To quantify the added clinical value of 3CB
65 imaging, we compared the performance of CAD based models to identify malignancies without and with 3CB lesion
66 characterization. Malignant and non-malignant masses and hormone receptor status were further studied to better
67 understand the biological mechanism which led to increased specificity of models that include 3CB composition.

68

69 **RESULTS**

70 **Data acquisition**

71 Three hundred ninety-five women who were scheduled for breast biopsy for suspicious lesions (Breast Imaging-
72 Reporting and Data System (BI-RADS) diagnostic categories 4 and 5) were recruited at the University of California
73 San Francisco (San Francisco, CA) and H. Lee Moffitt Cancer Center and Research Institute (Tampa, FL). In
74 addition to clinical diagnostic mammograms, participants underwent further research imaging using the 3CB
75 protocol prior to breast biopsy. FFDMs were acquired on Hologic Selenia systems (Hologic, Inc. Bedford, MA). In
76 brief, the 3CB imaging protocol consisted of two images in succession: a clinical mammogram (autocontrast, auto
77 compression release off) and a high energy (HE) image acquired at 39 kVp (40 mAs, 3-mm additional aluminum
78 filtration). A calibration phantom was placed on top of the breast compression paddle during imaging to accurately
79 estimate paddles compression depth, warp, and tilt from which exact submillimeter point thicknesses of the breast
80 could be calculated.³¹ With these three pieces of information (HE attenuation, low energy LE attenuation, and local

81 breast thickness) a system of three equations was solved which resulted in the LWP thicknesses at each pixel.
82 Absolute accuracy of this technique has been previously verified using reference standards.^{19,32}

83 Pathology results were reported on all biopsies and radiologist delineated the mammographic abnormalities on
84 presentation mammogram images. This work reports on results from 349 participants after exclusions. Participants
85 were excluded if biopsy site annotation coordinates could not be correctly registered on presentation or 3CB images,
86 if lesion pathology was incomplete, or if the 3CB data set was incomplete. The 3CB protocol requires that images
87 be acquired on calibration objects prior to patient imaging and the absence of calibration images or poor image
88 quality, due to excessive movement between HE and LE image acquisition, resulted in an incomplete 3CB data set
89 and exclusion.

90 Participants were imaged in both the craniocaudal (CC) and mediolateral oblique (MLO) views which resulted in
91 698 images of 349 women participants. Images were excluded if any of the 3CB images contained. After image
92 exclusion, 660 images remained which contained a total of 689 radiologist delineated regions of interest (ROIs) of
93 biopsy sites for which pathology was reported. The 689 ROIs consisted of 103 invasive ductal carcinoma (IDC), 61
94 ductal carcinoma in-situ (DCIS), 116 fibroadenomas (FA), and 409 other benign (BN), see Figure 1a. Figure 1b
95 contains details of participants by age, body mass index (BMI), BI-RADS breast density score, and duration of
96 hormone therapy. Figure 1c stratifies ROIs by BI-RADS density categories.

97 **3CB feature extraction**

98 The corresponding 3CB LWP thickness maps were generated for all 660 FFDM images and were used to quantify
99 the composition within the radiologist delineated ROIs. Standard presentation images and the corresponding 3CB
100 composition maps can be observed in Figure 2a. Note that the 3CB images are thickness maps where each pixel
101 corresponds to a thickness, in centimeters, of a given composition. To abstract compositional information away
102 from morphological features, we computationally extracted nine measurements to quantify the composition within
103 a given region. These nine measurements included the mean, median, standard deviation, minimum, maximum,
104 kurtosis, skew, total and percentage value of all pixels contained within a ROI.

105 Three additional outer ROIs were derived from the lesion ROI to capture the background or tissue immediately
106 surrounding a lesion, see Figure 2b. Each outer region captured all pixels extending 2mm from the border of the
107 previous region. Therefore, the first, second, and third outer regions contain all pixels extending from the edge of
108 the lesion ROI out to 2mm, the edge of the first outer region out to 2mm, and the edge of the second outer region
109 out to 2mm, respectively. In other words, in relation to the lesion border, the first, second, and third outer regions
110 measure 0 to 2mm, 2mm to 4mm, and 4mm to 6mm, respectively. For each lesion, we obtained nine compositional
111 measurements from four ROIs (lesion and three outer regions) on each of the three compositional images (3CB
112 LWP maps) which resulted in 108 compositional features per lesion ROI.

113 **Clinical CAD lesion detection**

114 Low energy, standard FFDMs were processed using commercial CAD software (SecondLook, version 7.2, iCAD,
115 Nashua, NH) to identify suspicious masses and calcifications. The CAD software utilizes a proprietary algorithm
116 to delineate suspicious ROIs for masses and individual calcifications as well as assigns a probability of malignancy
117 for each delineation. Note that for input to our analysis, we used the calcification cluster ROI rather than each
118 individual calcification ROI. Calcification cluster ROIs were calculated using the convex hull or minimum envelope
119 which encompasses all calcifications associated with a cluster. Therefore, CAD delineated ROIs, used in our final
120 analysis, may consist of either a suspicious mass or a calcification cluster.

121 From 660 images, CAD delineated 1187 ROIs. Only 418 CAD delineated ROIs had a 25% or greater overlap with
122 the radiologist delineated biopsy sites. Overlapping ROIs were included in the modeling dataset and the 108, 3CB
123 features were extracted for each ROI. See Figure 1a.

124 The 769 non-overlapping CAD ROIs were excluded from our analysis because they did not overlap biopsy sites
125 and thus, pathology diagnosis could not be confirmed. Of the patients with DCIS pathologies, CAD failed to
126 delineate any ROI on one patient resulting in a complete miss. CAD missed one delineation for the CC view for
127 one patient and missed another delineation on the MLO view for another patient. In total, four DCIS ROIs were not
128 identified by CAD. Of patients with IDC pathologies, CAD completely missed delineations on seven patients,

129 missed three delineations on the MLO view, and one delineation for the CC view. In total, 18 IDC lesions were not
130 identified by CAD but were delineated by the radiologists and are present in the final data set.

131 **Predictive modeling with morphology and 3CB**

132 The final dataset, consisting of 1107 ROIs (689 radiologist and 418 CAD delineated, see Figure 1a) from 349
133 patients, was split by patient into a train, validation, and test set using a 60%, 20%, 20% split. The data was split by
134 patient ID such that all ROIs for a given patient remained exclusively in one of the three datasets. This data split
135 condition ensured no data leakage and ROIs from a single patient, which are highly correlated, did not end up in
136 both the training and test set, for example. To reiterate, the train, validations, and test data sets contained their own
137 unique subset of patients and patient ROIs and the test set contained 20% of the patients.

138 A neural network model was trained to predict malignancy probability from the 108 extracted 3CB features and the
139 prediction from CAD. CAD predicts probabilities of malignancy rather than specific lesion type. To compare
140 against CAD performance, target labels were created for our dataset which combined BN and FA pathologies into
141 a non-malignant label. ROIs with DCIS and IDC pathologies were also combined into a new malignant label. The
142 final model was trained to output these new targets or probability of malignancy.

143 On the unseen, independent hold out test set, the commercial CAD output of probability of malignancy resulted in
144 a mean area under the receiver operating characteristic (ROC) curve of 0.69 and a 95% confidence interval (CI) of
145 0.60-0.78. On this same test set, the neural network model, which utilized both morphological features captured by
146 CAD and compositional features derived from 3CB, resulted in a mean area under the curve (AUC) of 0.81 and CI
147 of 0.74-0.87. Bootstrapping (1000 bootstrap samples) was used to calculate the mean AUC and 95% confidence
148 intervals for ROC curve presented in Figure 3a.

149 **Quantifying the added diagnostic benefit of 3CB for malignancy prediction**

150 To quantify the added value of 3CB's compositional information to information derived from standard clinical
151 imaging, we calculated the integrated discrimination improvement (IDI) and net reclassification improvement (NRI)
152 of malignancy prediction^{33,34}. IDI and NRI offer additional insight into the benefits of new biomarkers by evaluating

153 performance differences, across all calculated risks, between a reference model and a new model, which contains
154 the added biomarkers. The NRI measures the number of cases correctly reclassified by the new model while the
155 IDI also takes into account the magnitude of the change of the newly calculated risk. In Figure 3b, CAD (dashed
156 lines) and CAD+3CB (solid lines) represent the reference and new model, respectively with the malignancies as
157 black and non-malignancies as red. In the ideal case, the addition of a useful biomarker(s) would improve
158 classification of events resulting in upward movement of the black solid line relative to the black dashed line³³. The
159 inverse is true for non-events and the addition of a useful biomarker results in downward movement of the solid
160 read line relative to the dashed read line. The IDI is represented by the shaded regions between the reference and
161 new model or the area between the solid and dashed lines for events and non-events. The IDI for events is -1.1%,
162 for non-events is 13.2%, and the overall IDI, which is the summation of all IDI events and non-events, is 12.1%.

163 Figure 3b also allows for the investigation of lesion reclassification with respect to BI-RADS assessment categories.
164 Vertical dash lines indicate the border between BI-RADS categories. From left to right the lines indicate the BI-
165 RADS 3/4a, 4a/4b, 4b/4c, 4c/5 borders at risk threshold of 2%, 10%, 50%, and 95%³⁵, respectively. NRIs for events
166 and non-events were calculated at each BI-RADs risk threshold. For all events or malignant lesions, a positive NRI
167 indicates that the new model, which includes 3CB, more correctly predicted a lesion's malignancy probability
168 resulting in a higher score. For non-events or benign lesions, a positive NRI indicates that the new model correctly
169 changed a lesion's malignancy probability from a higher to lower score. The total NRI for a given threshold is the
170 summation of the events and non-events NRIs. The total NRI at each BI-RADs risk threshold (3/4a, 4a/4b, 4b/4c,
171 4c/5) is 4%, 15%, 29%, and -28%. The overall NRI, which is the summation of all NRI events and non-events
172 across all thresholds, is 25%. A breakdown of each test set ROIs classification by both reference and new models
173 as well as their NRIs are presented in Figure 3c.

174 **Lesion composition characterization**

175 Evidence demonstrates that malignant, particularly IDC, lesions have unique biological and compositional
176 characteristics which may have contributed to better model performance. To investigate further, 3CB thickness heat
177 maps for lesions of each type (BN, FA, DCIS, IDC) which resulted in high NRIs were generated for Figure 4. Using

178 the visible light color spectrum ordering convention, red indicates higher quantities of a given tissue component
179 and quantities decrease as colors move towards violet. All lesion types, except DCIS, appear to have higher
180 concentrations of protein and water relative to their background or surrounding tissue. Additionally, all lesions
181 appear to have less lipid than surrounding parenchyma, and invasive lesions contain considerably less lipid
182 compared to their surroundings. The invasive lesions in particular appear to have a noticeably higher water signal.

183 Using quantitative methods, we further investigate compositional differences amongst the four different lesion
184 pathologies. To quantify these unique signatures the median LWP values from each of the surrounding outer region
185 ROIs was subtracted from the median LWP values from within the lesion ROI. Only radiologist drawn ROIs
186 delineating biopsy sites were included in this analysis, $R=689$. Microcalcifications are present in many of the
187 mammograms and although they are not composed of lipid, water, or protein, they can produce a high water and
188 protein signal in the 3CB thickness maps. Therefore, the median pixel values were used to mitigate the influence
189 microcalcifications have on the mean composition within an ROI. Lesion differences were stratified by pathology
190 and compositional component type (i.e. lipid, water, or protein) and comparisons are shown in Figure 5a.

191 Figure 5a shows that all lesions contain less lipid when compared to their background as indicated by negative
192 median values in the box and whisker plots. The IDC lipid signature is strongest and distinctly different than the
193 other lesion types. BN, FA, and DCIS lesions tend to have less water when compared to the surrounding tissue
194 however IDC lesions show an increase in water content. All lesion types have a higher protein signature when
195 compared to the three outer surrounding regions and IDC lesions show the largest signature. As demonstrated by
196 the circumferential regions of interest, the protein content increases from the background reaching a peak in the
197 lesion itself.

198 Our model predicts probability of malignancy rather than lesion type, so malignant and non-malignant types were
199 grouped for this analysis. The orange dashed line represents the average signature for malignant lesion types (DCIS
200 and IDC) and the blue dashed line indicates the average signature between non-malignant types (BN and FA).
201 Differences between the malignant and non-malignant compositions are indicated by the space between the blue
202 and orange lines. This difference is also quantified and presented in Figure 6. Malignant lesions have a lower lipid,

203 higher water, and higher protein signature when compared to non-malignant types. Compositional difference
204 between malignant and non-malignant lesions amplifies when moving further out into the surrounding tissue or
205 towards outer region 3. All compositional differences between malignant and non-malignant lesions result in
206 significant p-values, see Figure 5b.

207 Lastly, we look at possible correlations between invasive cancers and patient hormone receptor status. It is
208 hypothesized that cancers of different receptor type have unique compositional signatures due to utilization of
209 exogenous fatty acids for sustained growth^{26,36,37}. To investigate, we compared the composition of IDC lesions to
210 their background and stratified each lesion by hormone receptor status (Figure 6). The orange dot-dashed line
211 indicates triple negative lesions, and the blue dashed line represents all receptor positive lesions; estrogen receptor,
212 progesterone receptor, human epidermal growth factor receptor 2 or any combination of the three. The lipid content
213 of triple negative cancers is less than the lipid content of hormone receptor positive cancers for the second and third
214 outer regions as indicated by the space between the orange and blue lines in Figure 6. Water and protein content of
215 triple negative cancers also appear to be distinctly different than hormone positive cancers and that difference
216 increases the further away we get from the lesion (i.e. the difference when evaluating the surrounding tissue 2mm
217 away from the lesion is smaller than when evaluating the region 6mm away from the lesion). This indicates a
218 gradient difference in the lipid and water content of the surrounding tissue for triple negative cancers. The change
219 in the vertical position of the orange and blue lines across the three graph columns further demonstrates this gradient
220 and suggest that receptor positive cancers have different compositional gradients than triple negative cancers.

221

222 **DISCUSSION**

223 This work suggests further support to the hypothesis that different breast lesion pathologies result in unique LWP
224 compositions that can be directly measured through our novel 3CB, dual-energy mammography technique. We
225 developed a neural network model to empirically demonstrate that adding compositional information improves
226 classification of malignant and non-malignant lesions, providing diagnostic value. Further investigation into 3CB-

227 derived features revealed distinct differences between lesions and their surrounding parenchyma composition,
228 mechanisms that likely contribute to the increased predictive performance.

229 Previous work showed that compositional features were predictive of lesion pathology and models could be built
230 to reasonably identify malignancies from composition alone.³⁸ Like trained radiologists, CAD software only has
231 morphology, texture, and image opacity available to make malignancy probability decisions. When combining these
232 morphologic features with compositional features from 3CB in our neural network model, the AUC on the test set
233 increased. The IDI and NRI analysis showed that the boost in AUC is attributed to increased specificity via the
234 reduction of false positives or lowering malignancy probability on non-malignant lesions that CAD had previously
235 assigned a high probability. The potential reduction in false positives is highlighted by the large red area between
236 the new and reference models in Figure 3b. The addition of 3CB features also resulted in more accurate BI-RADS
237 classification of malignant lesions and reclassification to lower BI-RADS categories for non-malignant lesions thus
238 demonstrating an increase in confidence levels with respects to the decision to biopsy. Using 3CB imaging to
239 increase specificity has the potential to be clinically beneficial with only minimal additional risk (10% additional
240 dose from the acquisition of a second, high-energy, mammogram). It should also be noted that this method of
241 obtaining useful compositional information, unlike CEM, does not require contrast agents and the possibility of
242 adverse reactions to contrast is non-existent.

243 Comparing compositional differences between lesions and their background supports the hypothesis different lesion
244 pathologies present unique 3CB signatures. The aggressive biological nature of invasive lesions causes them to
245 consume lipids at a high rate, and this phenomenon was observed on a microscope scale with 3CB imaging. IDC's
246 lower levels of lipid compared to surrounding tissue, observed in Figure 5a, is consistent with the literature. The
247 lipid signature, which is the difference between the lesion and its surrounding region, increases as the region of
248 comparison is moved further away from the lesion border. This further supports the aggressive growth natures of
249 invasive cancers in that it begins to metabolize lipid from its peripheries. While non-malignant lesions were
250 significantly different from malignant lesions for all composition types (LWP), it is likely that predictions were
251 primarily driven by the lipid compositions since that signature is the greatest. There is a positive correlation between

252 the magnitude of each compositional signature and the distance away from the lesion border. In other words, there
253 is a gradient difference in tissue composition such that the composition becomes more different than normal breast
254 tissue nearer the lesion. Although our models and analysis are focused on detection, gradient compositional changes
255 of the breast could be useful in a screening situation as well.

256 Recall, 108 3CB features were purposely extracted from the image in order to abstract the compositional
257 information away from morphology. However, the entire 3CB thickness maps of LWP affords more information,
258 on many orders of magnitude, than what was captured by the 108 features we used. In addition, there are more
259 powerful computer vision methods such as convolutional neural networks which could potentially open the door to
260 better automated detection and screening with 3CB images.

261 A reader study demonstrated CAD's ability to improve radiologists' ability to detect breast cancers³⁹. Since we
262 demonstrated improvements to CAD prediction with 3CB, it is reasonable to presume that the addition of 3CB
263 would also further improve radiologists' ability to accurately detect and classify lesions. The translational clinical
264 benefit of 3CB is the increased confidence in the decision to biopsy which has the potential to reduce unnecessary
265 biopsies.

266

267 **METHODS**

268 **3CB Imaging**

269 All images were acquired from women scheduled for percutaneous breast biopsy, prior to their biopsy. We used a
270 single Hologic Selenia full-field digital mammography system (Hologic, Inc. Bedford, MA) to image women with
271 3CB. This particular system configuration has a molybdenum X-ray anode and two internal X-ray filters of either
272 Molybdenum or Rhodium. Two mammograms were acquired on each woman's affected breast using a single
273 compression. The first exposure was made to mimic the clinical screening mammogram conditions such that the
274 Selenia's internal software chooses the voltage and current settings based on breast thickness usually below 30 kVp.
275 The second mammogram was acquired at a fixed voltage (39 kVp) and current for all participants. An additional 3-

276 mm thick X-ray filter was placed in the beam path to remove more of the low energy X-rays. A high energy exposure
277 (39 kVp/Rh filter) was made using an additional 3-mm plate of copper in the beam to increase the average energy
278 of the high energy image. The 39 kVp high-energy voltage is the highest obtainable voltage on the Selenia unit. We
279 limited the total dose of this procedure to be approximately 110% of the mean-glandular dose of an average
280 screening mammogram. The images were collected under an investigational review board approval to measure
281 breast composition. The calibration standards and 3CB algorithms for generating compositional thickness maps
282 have been previously described in full^{32,40}.

283 **Lesion Diagnosis**

284 Pathology was reported on all biopsied lesions at both clinical sites (University of California, San Francisco, San
285 Francisco, Calif, and H. Lee Moffitt Cancer Center, Tampa, Fla) to determine ground truth diagnosis. Hormone
286 receptor assays were performed on lesions with malignant pathologies to identify estrogen receptor, progesterone
287 receptor, and human epithelial receptor 2 status.

288 **Biopsy Site Delineations**

289 Sub-specialized breast radiologists at both clinical sites used pre-biopsy mammograms and pathology reports to
290 delineate the site of the biopsy. Custom software was used to capture the delineations and store the x and y
291 coordinates of each delineation point. Medical grade, high resolution radiology monitors were used for viewing and
292 delineations. Presentation images used for radiologist readings and delineations are co-registered with the resulting
293 3CB thickness maps. Therefore, the delineation coordinates will be projected in the exact location on all 3CB
294 thickness maps.

295 **CAD Delineations**

296 Patients' diagnostic mammograms, in raw DICOM format, were pushed to a local iCAD PowerLook server running
297 CAD software. Using iCADs CAD proprietary algorithm at the most sensitive setting, the iCAD delineate
298 suspicious masses and each individual calcification within a calcification cluster. CAD also assigned a probability
299 of malignancy for each suspicious mass and calcification cluster. The x and y coordinates of each CAD delineation
300 was captured and stored in an output Extensible Markup Language (XML) file.

301

302 Some patients present with numerous calcifications and the total number of individual calcifications significantly
303 outnumber the total number of masses identified by CAD. In order to address this possible imbalance, new
304 delineations were generated which delineated an ROI for a calcification cluster rather than use the delineation for
305 all individual calcifications. CAD automatically indexed and grouped each calcification. The new ROI was
306 calculated by taking all calcification within a cluster, extracting the set of x and y coordinates, and calculating the
307 convex hull for that set of all coordinates^{41,42}.

308 **3CB Feature Engineering**

309 Three outer region ROIs were generated around the lesion ROI to evaluate the area and tissue immediately
310 surrounding a lesion. Each outer region ROI was 2mm in thickness and thus 2mm away from the border of the
311 previous ROI. Using the lesion ROI coordinates, a Euclidean distance transform⁴² was used to compute coordinates
312 2mm away from the lesion border, for the first outer region. This same method was used to compute the second
313 outer region and third outer region by using the first outer region and second outer region as the reference points
314 for the Euclidean distance transform respectively. As a result, each lesion has a total of four ROIs; one for the lesion
315 and three outer regions 2mm in thickness at distances of 2, 4, and 6mm from the lesion ROI, see Figure 2b.

316 Single numeric values, which includes mean, median, standard deviation, minimum, maximum, kurtosis, skew,
317 total and percentage, were captured to characterize each ROI. These nine values were calculated for all four lesion
318 ROIs on each of the three 3CB thickness maps. A total of 108 total compositional features were extracted from
319 every single lesion.

320 **Data Augmentation**

321 To combat overfitting of our model, data augmentation was implemented at the level of ROI delineations. The 3CB
322 thickness maps contain the point thicknesses of a given composition (LWP) on a pixel by pixel basis and the 108
323 extracted features are derived from all pixels within an ROI. It is unlikely that an ROI delineation perfectly captures
324 all pixels corresponding to a lesion while perfectly excluding pixels corresponding to normal breast tissue. In
325 addition, human variability explains that delineation ROIs for the same lesion will not result in the exact same
326 coordinates despite delineations originating from the same radiologist. Therefore, our augmentation strategy was
327 meant to account for possible variability involved with delineating ROIs. ROIs were rotated within a range 10

328 degree and translated in any direction within a range of five pixels. Rotation and translation augmentations were
329 not mutually exclusive, and a new augmented ROI could have undergone both transformations. Features were
330 extracted from all newly augmented ROIs and included into the training set. This augmentation was performed as
331 a preprocessing step as opposed to during training. Augmentation ROIs only appeared in the training set and the
332 unseen test set for which results are report contained no augmentations.

333 **Modeling**

334 Our final predictive model was constructed with the Python programming language using the Keras machine
335 learning API. The neural network consisted of two main components. The first component consisted of five, 2048
336 node layers and it received the 108 extracted 3CB features from a lesion as input. The output from the first
337 component was used as input for the second component which consisted of two, 512 node layers. In addition to the
338 output from the first component, the second component also received CAD's predicted probability of malignancy
339 as input. A single node prediction layer, at the end of the second component, output a predicted the probability of
340 malignancy. The learning rate, decay, dropout, number of nodes, number of layers, and batch size were all optimized
341 and determined using the Sherpa, a hyperparameter optimization tool, population based genetic algorithm.^{43,44} The
342 search spaces for each optimized hyperparameter are as follows: between 1E-8 and 1 for learning rate, between 1E-
343 8 and 1 for decay, 0.1-0.9 for dropout, 128-2048 for number of nodes, 3-10 number of layers, and 2-512 for batch
344 size. The hyperparameter combination which resulted in the best AUC on the validation set was used to train the
345 final model. The best hyperparameters used in the final model are as follows: learning rate of 1.5E-5, decay of
346 5.18E-3, dropout of 0.2, 2048 nodes, 7 layers, and a batch size of 512. The final model was trained on the training
347 set and the model was frozen. The unseen test set was evaluated by the trained, frozen model, and those results are
348 reported in Figure 3.

349 **Statistics**

350 The Scikit Learn Python machine learning package was used to compute AUCs. The mean AUCs and
351 95% confidence intervals were computed via 1000 bootstrapping samples. The p-value significances in
352 Figure 5a and Figure 6 were calculated by Welch's test for unequal variance.

ACKNOWLEDGMENTS

The authors would like to thank the patients who participated in this study. The authors would also like to thank iCAD Inc. for providing the CAD server, software, and support. Lastly, the authors would like to acknowledge the National Cancer Institute No. R01 CA166945 grant and California Breast Cancer Research Program No. 18IB0042 for funding this study.

AUTHOR CONTRIBUTIONS

Developed the concepts and designed the study, JAS, KK, MLG; HG, scans interpretation and delineated biopsy sites, HG, BJ, BN; 3CB software development, SM, JAS; 3CB biomarker research and data analysis, LL, KD; data storage, upkeep, and curation, LL, TW; machine learning modeling and statistical analysis, LL, PS; manuscript drafting or manuscript revision for important intellectual content, all authors; approval of final version of submitted manuscript, all authors; agrees to ensure any questions related to the work are appropriately resolved, all authors.

COMPETING INTERESTS STATEMENT

Karen Drukker. Activities related to the present article: disclosed no relevant relationships. Activities not related to the present article: receives royalties from Hologic. Other relationships: disclosed no relevant relationships.

Maryellen Giger Activities related to the present article: disclosed no relevant relationships. Activities related to the present article: is a stockholder in R2/Hologic; is a co-founder in Quantitative Insights (now advisor to Qlarity Imaging); receives royalties from Hologic, GE Medical Systems, MEDIAN Technologies, Riverain Medical, Mitsubishi, and Toshiba; receives royalties through institution is a licensee on patents. Other relationships: disclosed no relevant relationships.

John Shepherd. Activities related to the present article: in kind equipment support from Hologic and iCAD. Activities not related to the present article: investigator-initiated grant from Hologic. Other relationships: disclosed no relevant relationships.

REFERENCES

1. Sung, H., *et al.* Global cancer statistics 2020: GLOBOCAN estimates of incidence and mortality worldwide for 36 cancers in 185 countries. *CA: A Cancer Journal for Clinicians* **n/a**.
2. Broeders, M., *et al.* The impact of mammographic screening on breast cancer mortality in Europe: a review of observational studies. *J Med Screen* **19 Suppl 1**, 14-25 (2012).
3. Hellquist, B.N., *et al.* Effectiveness of population-based service screening with mammography for women ages 40 to 49 years: evaluation of the Swedish Mammography Screening in Young Women (SCRY) cohort. *Cancer* **117**, 714-722 (2011).
4. Helvie, M.A., Chang, J.T., Hendrick, R.E. & Banerjee, M. Reduction in late-stage breast cancer incidence in the mammography era: Implications for overdiagnosis of invasive cancer. *Cancer* **120**, 2649-2656 (2014).
5. Myers, E.R., *et al.* Benefits and Harms of Breast Cancer Screening: A Systematic Review. *JAMA* **314**, 1615-1634 (2015).
6. Nelson, H.D., *et al.* in *Screening for Breast Cancer: A Systematic Review to Update the 2009 U.S. Preventive Services Task Force Recommendation* (Rockville (MD), 2016).
7. Lehman, C.D., *et al.* National performance benchmarks for modern screening digital mammography: update from the Breast Cancer Surveillance Consortium. *Radiology* **283**, 49-58 (2017).

8. Lee, C.S., Bhargavan-Chatfield, M., Burnside, E.S., Nagy, P. & Sickles, E.A. The national mammography database: Preliminary data. *American Journal of Roentgenology* **206**, 883-890 (2016).
9. Kerlikowske, K., *et al.* Comparative effectiveness of digital versus film-screen mammography in community practice in the United States: a cohort study. *Annals of internal medicine* **155**, 493-502 (2011).
10. Chong, A., Weinstein, S.P., McDonald, E.S. & Conant, E.F. Digital breast tomosynthesis: concepts and clinical practice. *Radiology* **292**, 1-14 (2019).
11. Lowry, K.P., *et al.* Screening performance of digital breast tomosynthesis vs digital mammography in community practice by patient age, screening round, and breast density. *JAMA network open* **3**, e2011792-e2011792 (2020).
12. Salomon, A. Beiträge zur Pathologie und Klinik der Mammakarzinome. *Arch Klin Chir* **101**, 573-668 (1913).
13. Giger, M.L., Chan, H.P. & Boone, J. Anniversary Paper: History and status of CAD and quantitative image analysis: The role of Medical Physics and AAPM. *Medical Physics* **35**, 5799-5820 (2008).
14. Jiang, Y.L., Nishikawa, R.M., Schmidt, R.A., Toledano, A.Y. & Doi, K. Potential of computer-aided diagnosis to reduce variability in radiologists' interpretations of mammograms depicting microcalcifications. *Radiology* **220**, 787-794 (2001).
15. Vyborny, C.J., Giger, M.L. & Nishikawa, R.M. Computer-aided detection and diagnosis of breast cancer. *Radiologic Clinics of North America* **38**, 725-740 (2000).
16. Lehman, C.D., *et al.* Diagnostic Accuracy of Digital Screening Mammography With and Without Computer-Aided Detection. *JAMA Internal Medicine* **175**, 1828-1837 (2015).
17. Dromain, C., Balleyguier, C., Adler, G., Garbay, J.R. & Delaloge, S. Contrast-enhanced digital mammography. *Eur J Radiol* **69**, 34-42 (2009).
18. Peters, N.H.G.M., *et al.* Meta-Analysis of MR Imaging in the Diagnosis of Breast Lesions. *Radiology* **246**, 116-124 (2008).
19. Avila, J., Malkov, S., Giger, M., Drukker, K. & Shepherd, J.A. Energy Dependence of Water and Lipid Calibration Materials for Three-Compartment Breast Imaging. in *International Workshop on Digital Mammography* 554-563 (Springer, 2016).
20. Drukker, K., *et al.* Mammographic quantitative image analysis and biologic image composition for breast lesion characterization and classification. *Medical physics* **41**, 031915 (2014).
21. Baumann, J., Sevinsky, C. & Conklin, D.S. Lipid biology of breast cancer. *Biochim Biophys Acta* **1831**, 1509-1517 (2013).
22. Menendez, J.A. & Lupu, R. Fatty acid synthase and the lipogenic phenotype in cancer pathogenesis. *Nat Rev Cancer* **7**, 763-777 (2007).
23. Huo, Z., Giger, M.L., Vyborny, C.J., Wolverson, D.E. & Metz, C.E. Computerized classification of benign and malignant masses on digitized mammograms: a study of robustness. *Acad Radiol* **7**, 1077-1084 (2000).
24. Weind, K.L., Maier, C.F., Rutt, B.K. & Moussa, M. Invasive carcinomas and fibroadenomas of the breast: comparison of microvessel distributions--implications for imaging modalities. *Radiology* **208**, 477-483 (1998).
25. Goodwin, P.J. & Chlebowski, R.T. Obesity and cancer: insights for clinicians. *Journal of Clinical Oncology* **34**, 4197 (2016).
26. Camarda, R., *et al.* Tumor cell-adipocyte gap junctions activate lipolysis and are essential for breast tumorigenesis. *bioRxiv*, 277939 (2018).
27. Cerussi, A., *et al.* In vivo absorption, scattering, and physiologic properties of 58 malignant breast tumors determined by broadband diffuse optical spectroscopy. *J Biomed Opt* **11**, 044005 (2006).
28. Chung, S.H., *et al.* In vivo water state measurements in breast cancer using broadband diffuse optical spectroscopy. *Phys Med Biol* **53**, 6713-6727 (2008).
29. Laidevant, A.D., Malkov, S., Flowers, C.I., Kerlikowske, K. & Shepherd, J.A. Compositional breast imaging using a dual-energy mammography protocol. *Medical physics* **37**, 164-174 (2010).

30. Drukker, K., *et al.* Combined Benefit of Quantitative Three-Compartment Breast Image Analysis and Mammography Radiomics in the Classification of Breast Masses in a Clinical Data Set. *Radiology Online First*(2018).
31. Malkov, S., Wang, J., Kerlikowske, K., Cummings, S.R. & Shepherd, J.A. Single x-ray absorptiometry method for the quantitative mammographic measure of fibroglandular tissue volume. *Med Phys* **36**, 5525-5536 (2009).
32. Malkov, S., *et al.* Calibration procedure of three component mammographic breast imaging. in *International Workshop on Digital Mammography* 211-218 (Springer, 2016).
33. Pencina, M.J., D'Agostino, R.B., Sr., D'Agostino, R.B., Jr. & Vasan, R.S. Evaluating the added predictive ability of a new marker: from area under the ROC curve to reclassification and beyond. *Stat Med* **27**, 157-172; discussion 207-112 (2008).
34. Pickering, J.W. & Endre, Z.H. New metrics for assessing diagnostic potential of candidate biomarkers. *Clinical Journal of the American Society of Nephrology* **7**, 1355-1364 (2012).
35. Sickles, E., *et al.* Acr bi-rads® mammography. *ACR BI-RADS® atlas, breast imaging reporting and data system* **5**, 2013 (2013).
36. Monaco, M.E. Fatty acid metabolism in breast cancer subtypes. *Oncotarget* **8**, 29487-29500 (2017).
37. Sun, X., *et al.* Metabolic Reprogramming in Triple-Negative Breast Cancer. *Front Oncol* **10**, 428 (2020).
38. Leong, L., *et al.* Three compartment breast machine learning model for improving computer-aided detection. in *15th International Workshop on Breast Imaging (IWBI2020)*, Vol. 11513 115130M (International Society for Optics and Photonics, 2020).
39. Conant, E.F., *et al.* Improving accuracy and efficiency with concurrent use of artificial intelligence for digital breast tomosynthesis. *Radiology: Artificial Intelligence* **1**, e180096 (2019).
40. Laidevant, A.D., Malkov, S., Flowers, C.I., Kerlikowske, K. & Shepherd, J.A. Compositional breast imaging using a dual-energy mammography protocol. *Med Phys* **37**, 164-174 (2010).
41. Graham, R.L. An efficient algorithm for determining the convex hull of a finite planar set. *Info. Pro. Lett.* **1**, 132-133 (1972).
42. Preparata, F.P. & Shamos, M.I. *Computational geometry: an introduction*, (Springer Science & Business Media, 2012).
43. Hertel, L., Collado, J., Sadowski, P. & Baldi, P. Sherpa: Hyperparameter Optimization for Machine Learning Models. (2018).
44. Jaderberg, M., *et al.* Population based training of neural networks. *arXiv preprint arXiv:1711.09846* (2017).

FIGURES

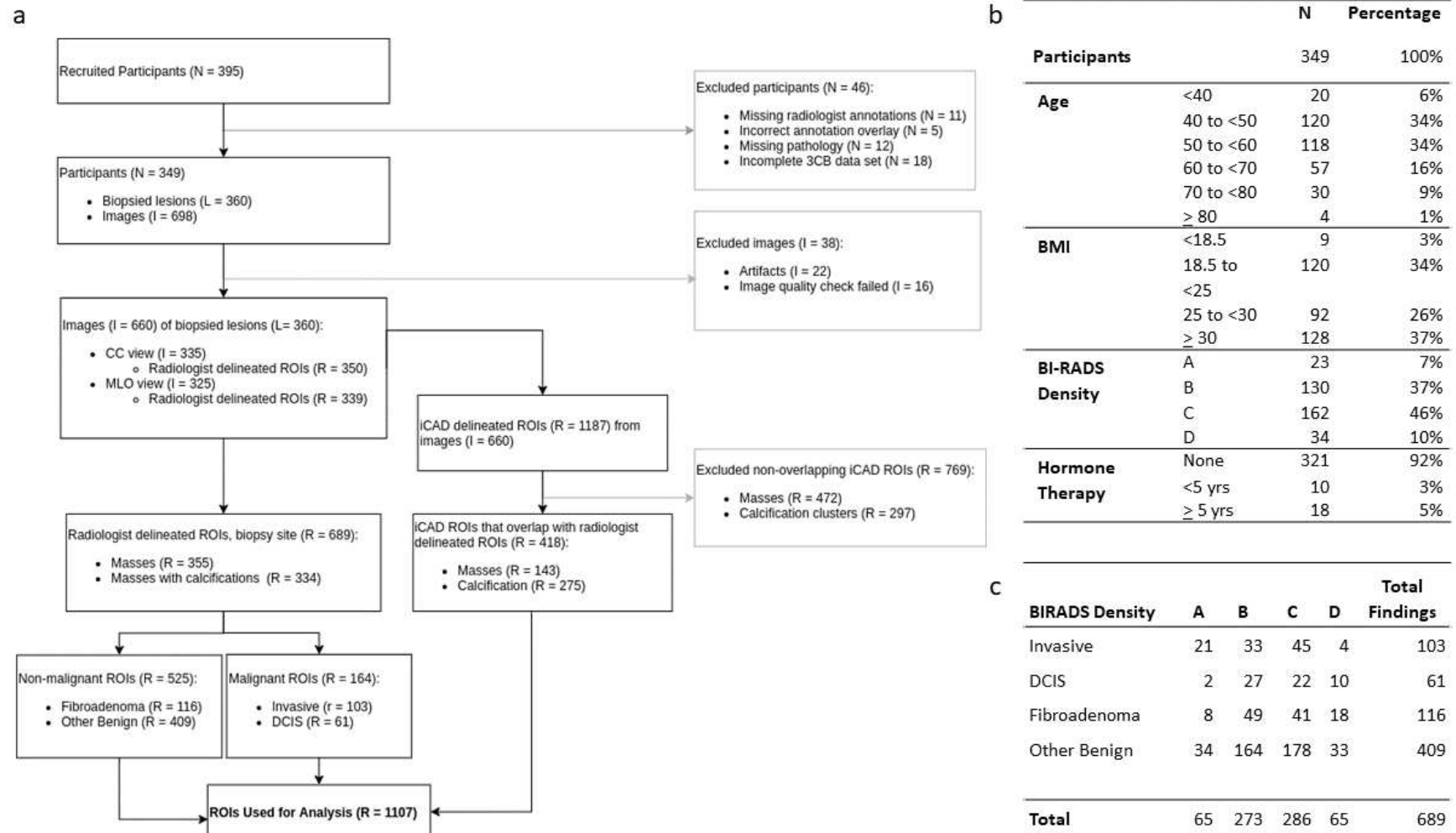


Figure 1. Overview of participants and data used for modeling and analysis. a, Flow diagram detailing inclusion and exclusion of data used in the final analysis. This study includes 349 patients (N) which equates to 360 biopsy sites (L) and 660 mammographic images (I) which includes CC and MLO views. The 660 images contained 689 radiologist delineated ROIs (R) and 413 CAD delineated ROIs agreed with radiologist delineated ROIs. The final data set contained all radiologist ROIs and agreeing CAD ROIs which results in 1107 ROIs. **b,** Participant stratification by age, BMI, BI-RADS density, and duration of hormone therapy. **c,** Separation of all 689 radiologist delineated ROIs by pathology and BI-RADS density.

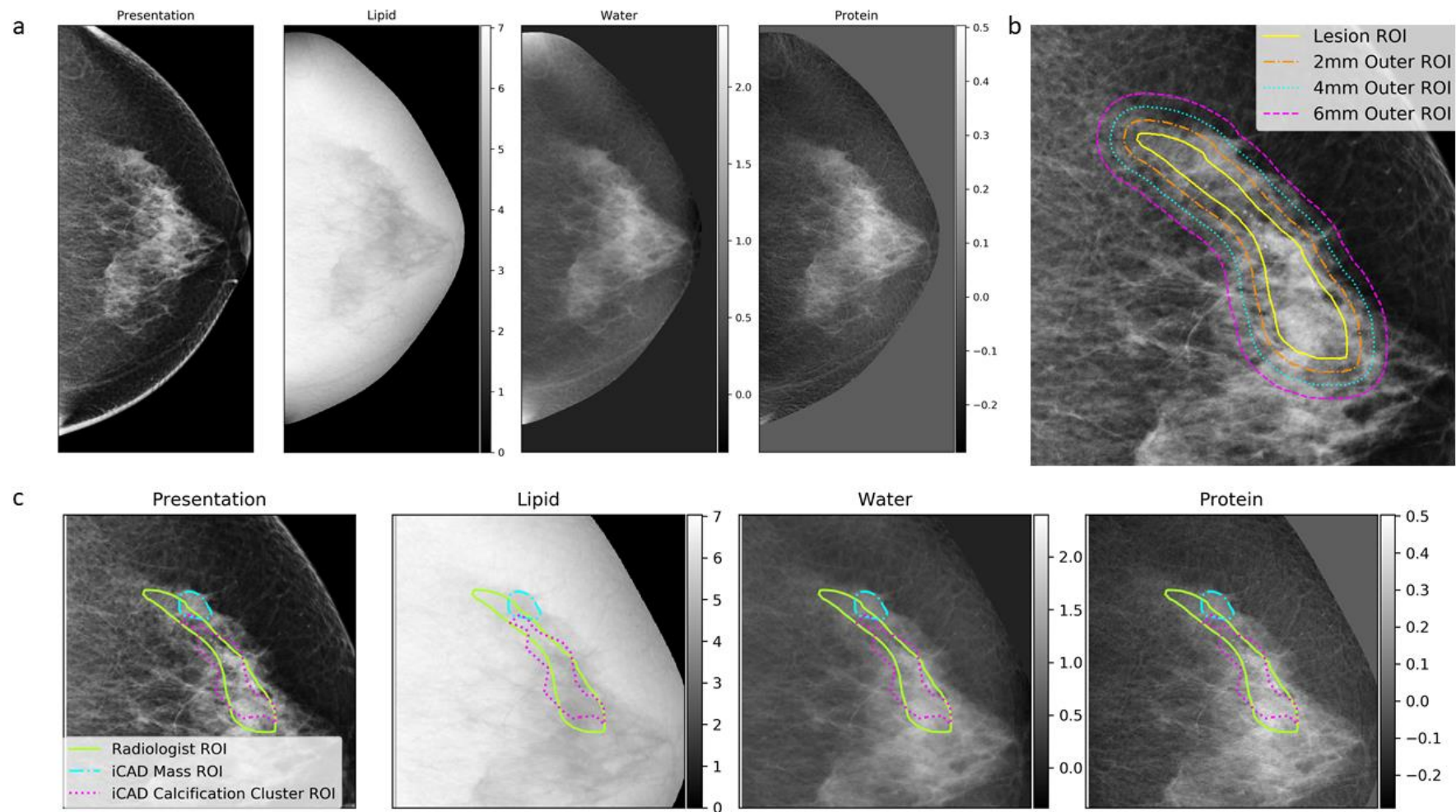


Figure 2. 3CB, lipid, water, and protein, data and regions of feature extraction. a, Full presentation mammogram image and the derived 3CB thickness maps. From left to right is the standard presentation craniocaudal mammogram used for reading by radiologist, lipid thickness map, water thickness map, and protein thickness map. Grayscale colorbars, adjacent to 3CB thickness maps, indicate thickness in cm. **b,** The composition of the background or tissue surrounding a lesion was measured progressively by capturing three outer regions extending from the border of the lesion (yellow solid line). The outer regions extend from the lesion border at distances of 2mm (orange dot-dashed line), 4mm (cyan dotted line), and 6mm (magenta dashed line). **c,** CAD delinations that had some agreement with radiologist ROIs (yellow line) were included in the final dataset. CAD delinates suspicious masses (cyan dot-dashed line) and calcification clusters (magenta dotted line). Outer regions for all ROIs (radiologist and CAD delineated) were calculated but not displayed in this sub-figure for easy viewing.

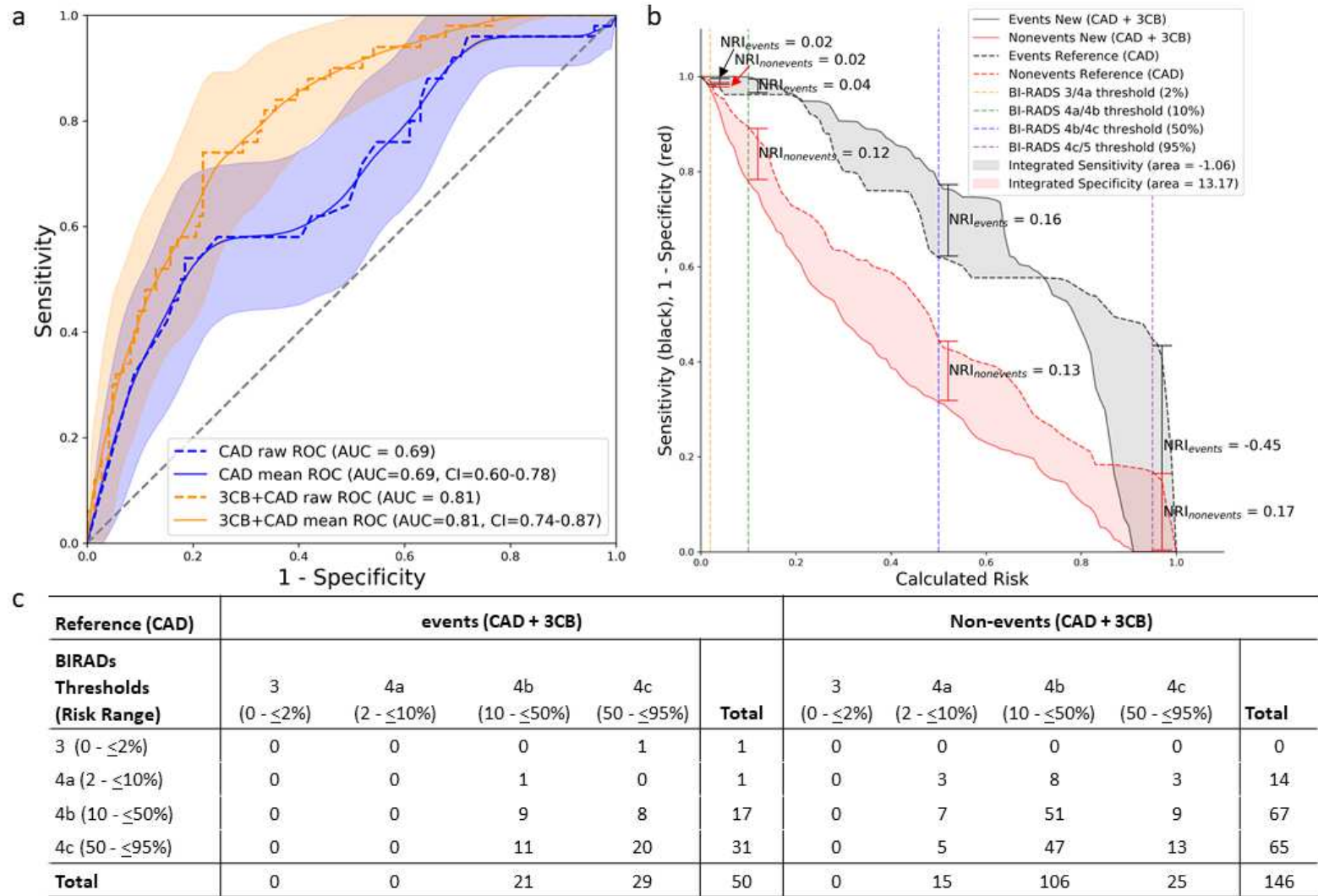


Figure 3. Improved performance on unseen test set when adding 3CB compositional information. **a**, Adding 3CB features to CAD (orange) results in an AUC of 0.81, STD of 0.03, when compared to CAD alone (blue), AUC of 0.69, STD of 0.04. Mean curves (solid lines) and 95% confidence intervals (shaded regions) were computed via 1000 bootstrap samples. **b**, The integrated sensitivity (IS), black shaded region between solid and dashed lines, indicates the change in sensitivity with the addition of 3CB. The integrated specificity (IP), red shaded region between solid and dashed lines, indicates the change in specificity with the addition of 3CB. The IDI is the sum of the IS and IP (-1.06 + 13.17) which is 12.11 and a positive IDI indicates that predictive models benefit from the addition of 3CB. The borders of the BI-RADS assessment categories are indicated by the vertical dashed lines. NRI for events or cancers (black) and non-events or benigns (red) are calculated at each BI-RADS border to demonstrate 3CBs effect on specificity with respects to each BI-RADS category. **c**, This table shows that adding 3CB allows for more accurate BI-RADS classification, as determined by probability of malignancy, for lesions with both malignant and non-malignant pathologies or events and non-events. The NRI for events and non-events is -0.02 and 0.25. The overall NRI, which is the sum of NRI events and non-events, is 0.25.

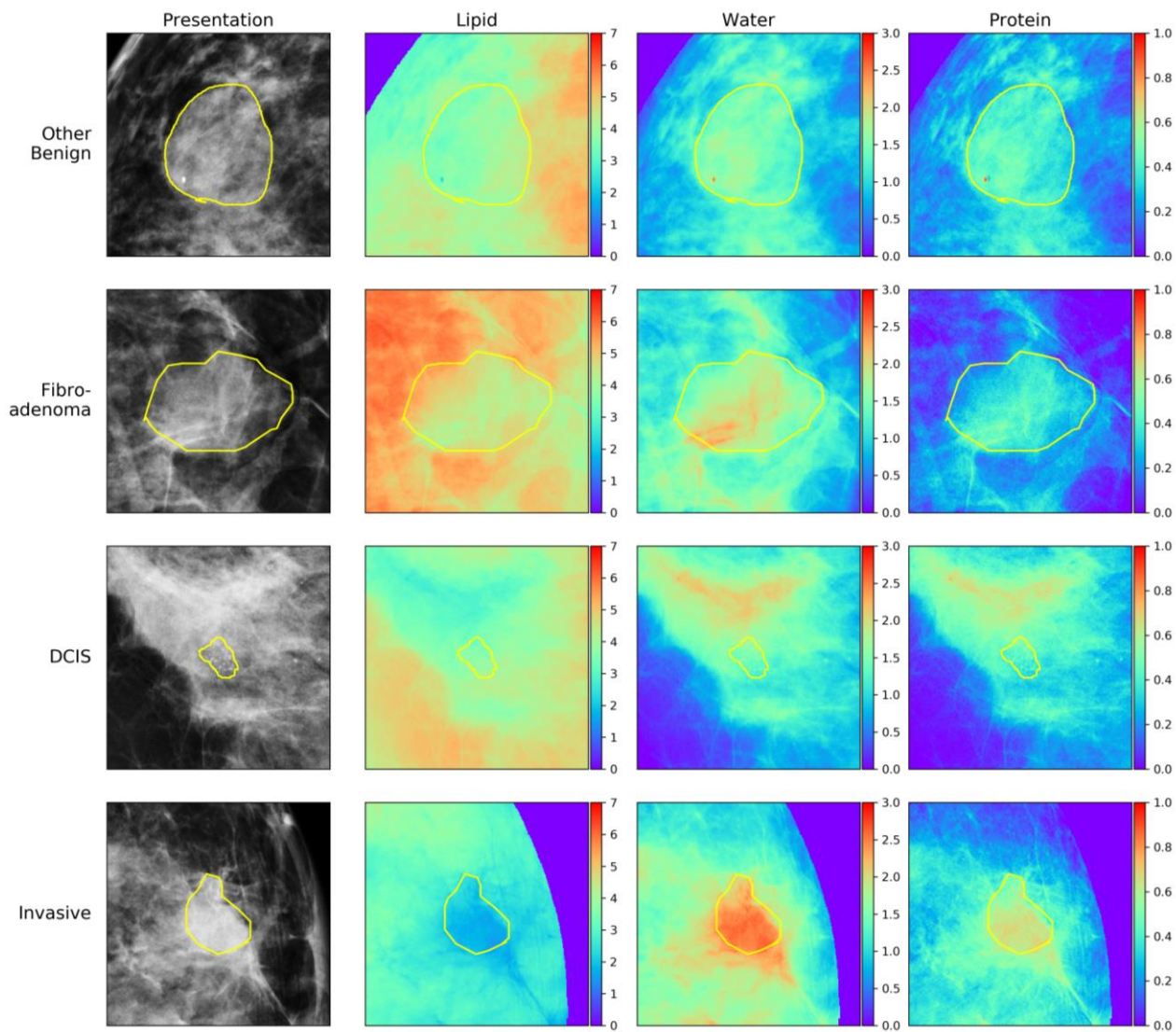


Figure 4. Compositional heatmaps of all lesion pathologies. Each row consists of a lesions with a different pathology. The first column contains the standard mammogram presentation, the second, third, and fourth columns contain the corresponding 3CB LWP thickness map. Colorbars adjacent to each 3CB map indicate thickness in cm where red indicates areas of high thickness and thickness decreases towards the color violet. Thickness ranges are normalized across each column. Yellow lines are radiologist delniations of where biopsies were taken from which lesion pathology was determined.

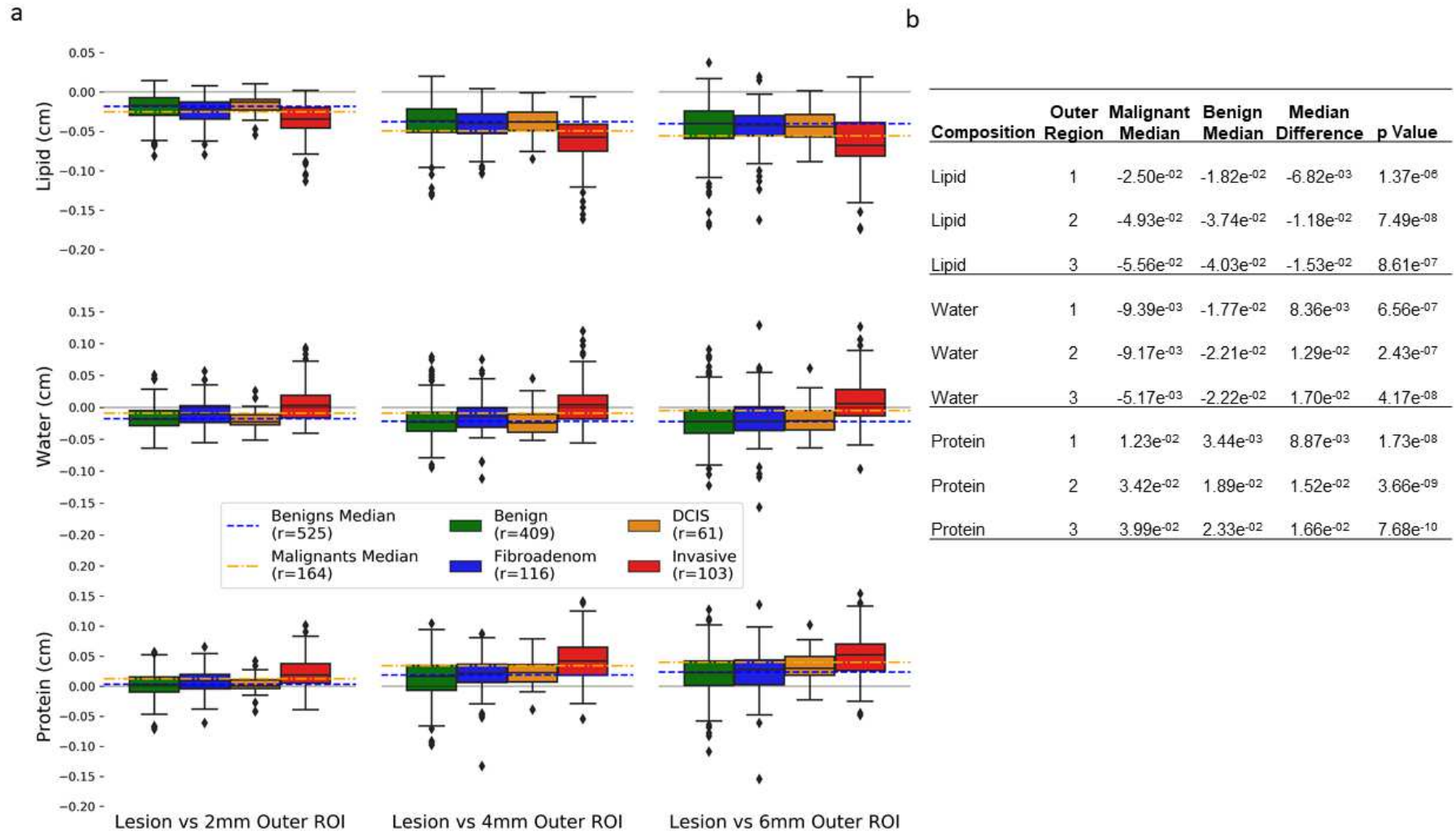


Figure 5. Lesion composition characterization. **a**, Differences between median composition values of the lesion and the outer regions were calculated for all radiologist ROIs. Column one, two, and three compares the composition within the lesion to the region 2mm, 4mm, and 6mm from its border respectively. Each row looks at a different compositional component, lipid, water, or protein. Calculated differences are stratified by the following lesion types; BN (green), FA (blue), DCIS (orange), and IDC (red). Median values of all benign lesions types, BN and FA, and malignant types, DCIS and IDC, are represented by blue and orange dashed lines respectively. Gray line indicates zero and ROIs that lay above this line have more of a given composition when compared to its corresponding background outer region. Boxes represent the 25 to 75% interquartile range and the center line represents the median. Whiskers represents 1.5 the interquartile range and outliers which fall outside that range are depicted as diamonds. **b**, Comparison between benign and malignant lesions compositions indicated by the space between blue and orange dashed lines in Figure 5a. are quantified in this table. P-values were calculated using a Welch’s test for unequal variance and all p-values are significant indicating that benign and malignant lesions have uniquely different compositions as measured by 3CB.

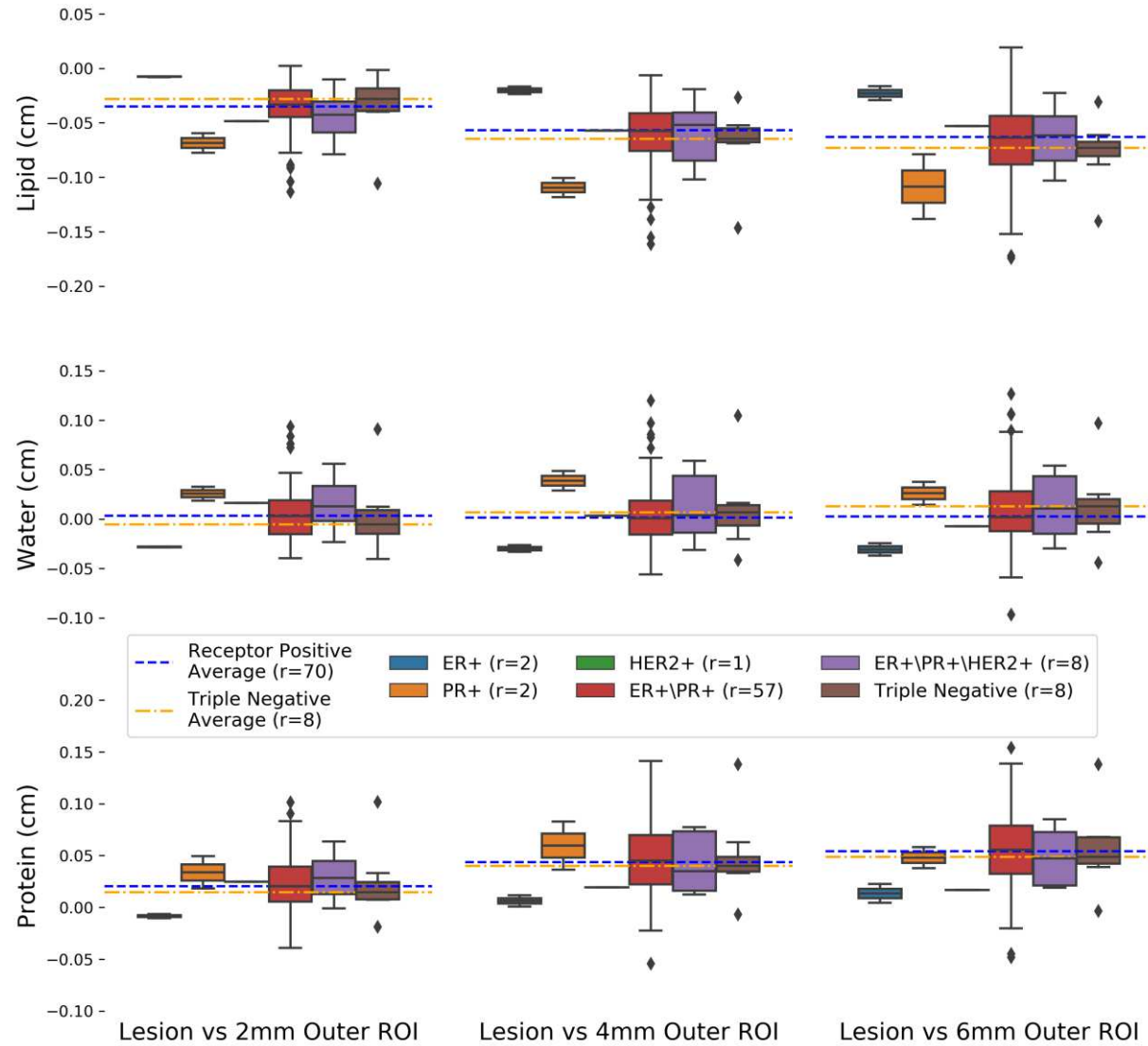


Figure 6. Hormone receptor composition characterization. Compositional difference between invasive lesions and their background are stratified by hormone receptor status. Median compositional difference between receptor positive and triple negative cancers are indicated by the blue and orange dashed lines respectively. Receptor positive median was calculated by including all lesion that contained either ER, PR, or HER2 receptor status.

Figures

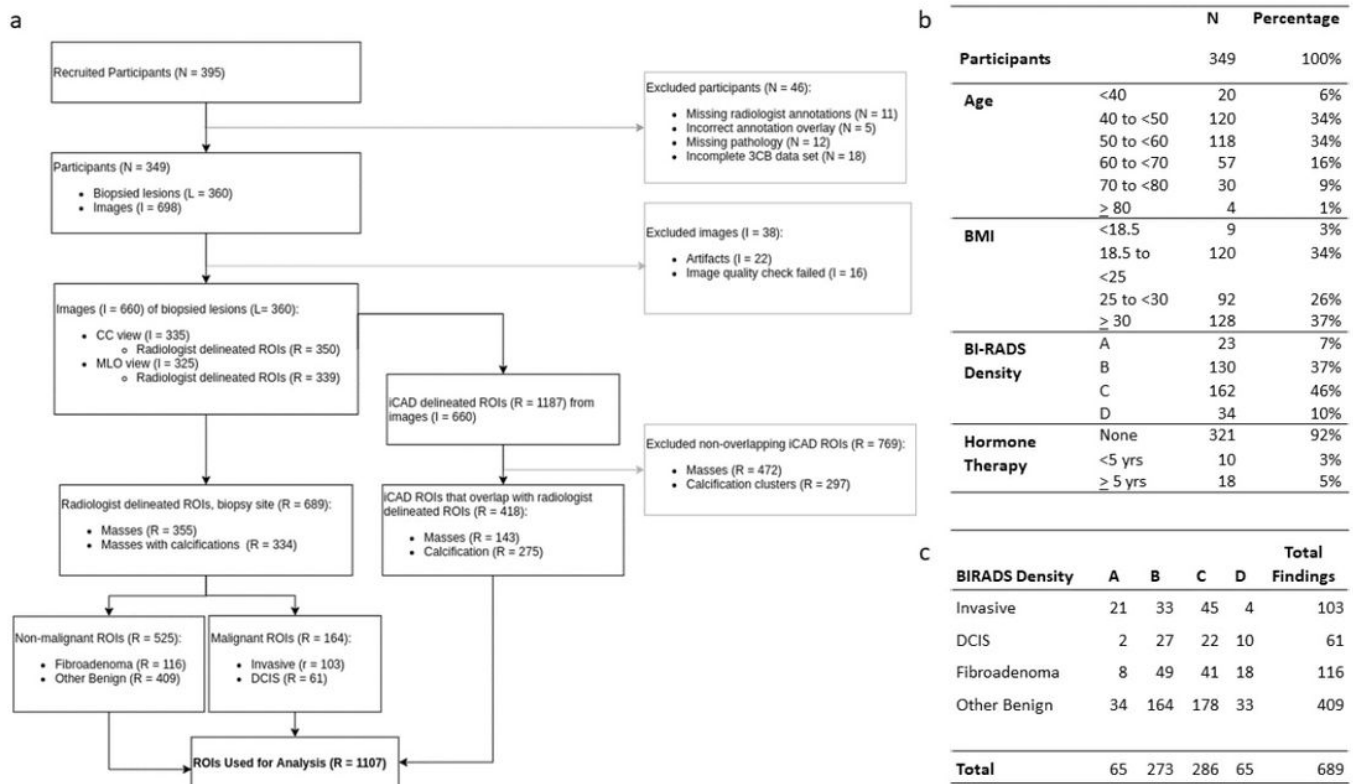


Figure 1

Overview of participants and data used for modeling and analysis. a, Flow diagram detailing inclusion and exclusion of data used in the final analysis. This study includes 349 patients (N) which equates to 360 biopsy sites (L) and 660 mammographic images (I) which includes CC and MLO views. The 660 images contained 689 radiologist delineated ROIs (R) and 413 CAD delineated ROIs agreed with radiologist delineated ROIs. The final data set contained all radiologist ROIs and agreeing CAD ROIs which results in 1107 ROIs. b, Participant stratification by age, BMI, BI-RADS density, and duration of hormone therapy. c, Separation of all 689 radiologist delineated ROIs by pathology and BI-RADS density.

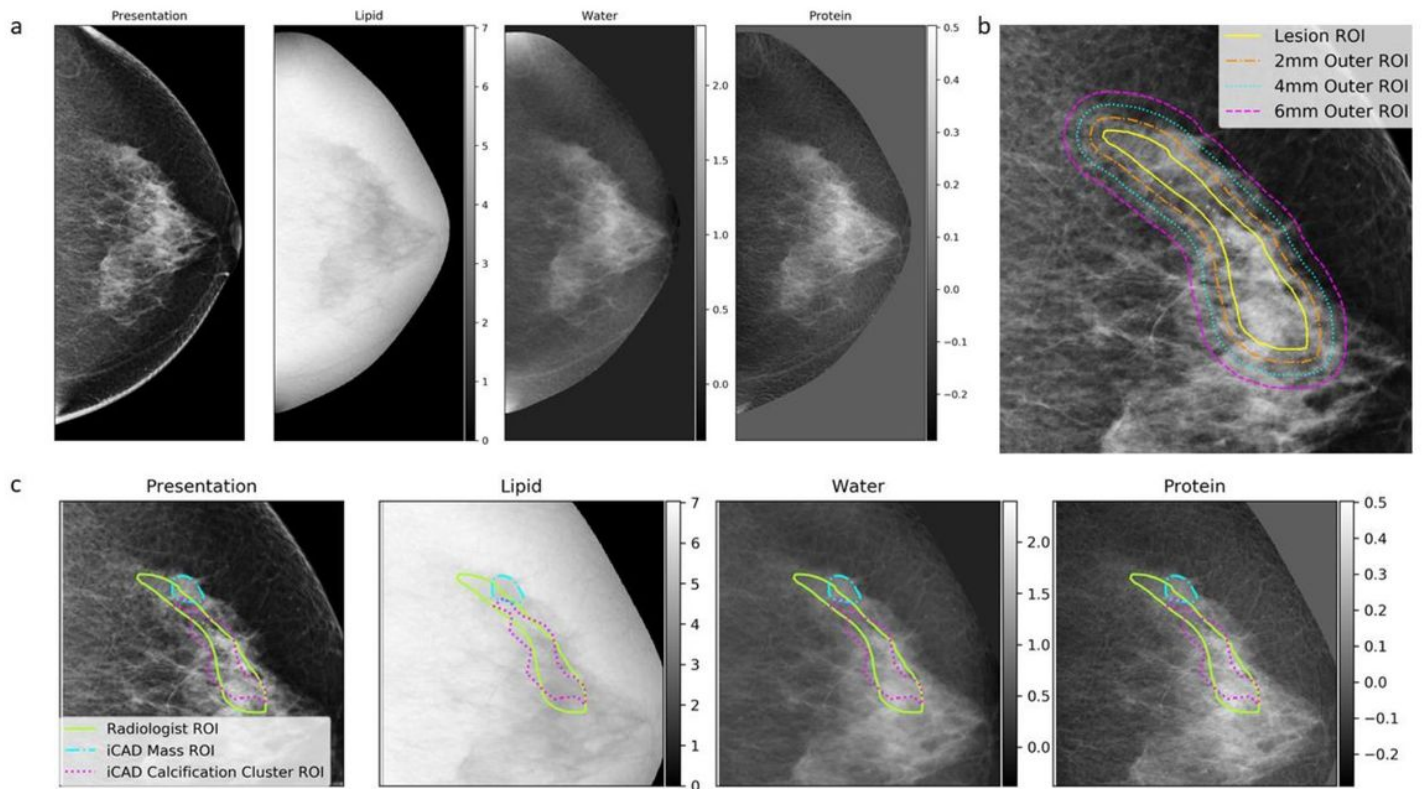
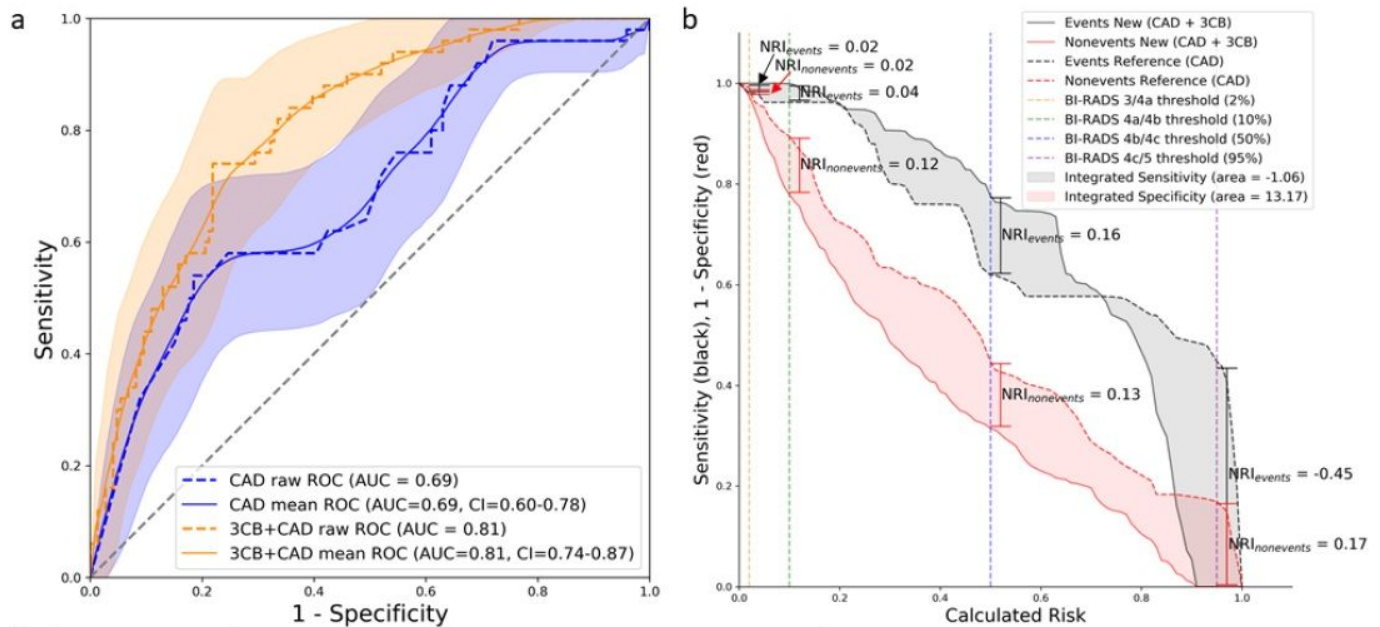


Figure 2

3CB, lipid, water, and protein, data and regions of feature extraction. a, Full presentation mammogram image and the derived 3CB thickness maps. From left to right is the standard presentation craniocaudal mammogram used for reading by radiologist, lipid thickness map, water thickness map, and protein thickness map. Grayscale colorbars, adjacent to 3CB thickness maps, indicate thickness in cm. b, The composition of the background or tissue surrounding a lesion was measured progressively by capturing three outer regions extending from the border of the lesion (yellow solid line). The outer regions extend from the lesion border at distances of 2mm (orange dot-dashed line), 4mm (cyan dotted line), and 6mm (magenta dashed line). c, CAD delinations that had some agreeance with radiologist ROIs (yellow line) were included in the final dataset. CAD delinates suspicious masses (cyan dot-dashed line) and calcification clusters (magenta dotted line). Outer regions for all ROIs (radiologist and CAD delineated) were calculated but not displayed in this sub-figure for easy viewing.



c

Reference (CAD)	events (CAD + 3CB)				Total	Non-events (CAD + 3CB)				Total
	3 (0 - <2%)	4a (2 - <10%)	4b (10 - <50%)	4c (50 - <95%)		3 (0 - <2%)	4a (2 - <10%)	4b (10 - <50%)	4c (50 - <95%)	
BIRADS										
Thresholds										
(Risk Range)										
3 (0 - <2%)	0	0	0	1	1	0	0	0	0	0
4a (2 - <10%)	0	0	1	0	1	0	3	8	3	14
4b (10 - <50%)	0	0	9	8	17	0	7	51	9	67
4c (50 - <95%)	0	0	11	20	31	0	5	47	13	65
Total	0	0	21	29	50	0	15	106	25	146

Figure 3

Improved performance on unseen test set when adding 3CB compositional information. a, Adding 3CB features to CAD (orange) results in an AUC of 0.81, STD of 0.03, when compared to CAD alone (blue), AUC of 0.69, STD of 0.04. Mean curves (solid lines) and 95% confidence intervals (shaded regions) were computed via 1000 bootstrap samples. b, The integrated sensitivity (IS), black shaded region between solid and dashed lines, indicates the change in sensitivity with the addition of 3CB. The integrated specificity (IP), red shaded region between solid and dashed lines, indicates the change in specificity with the addition of 3CB. The IDI is the sum of the IS and IP (-1.06 + 13.17) which is 12.11 and a positive IDI indicates that predictive models benefit from the addition of 3CB. The borders of the BI-RADS assessment categories are indicated by the vertical dashed lines. NRI for events or cancers (black) and non-events or benigns (red) are calculated at each BI-RADS border to demonstrate 3CBs effect on specificity with respects to each BI-RADS category. c, This table shows that adding 3CB allows for more accurate BI-RADS classification, as determined by probability of malignancy, for lesions with both malignant and non-malignant pathologies or events and non-events. The NRI for events and non-events is -0.02 and 0.25. The overall NRI, which is the sum of NRI events and non-events, is 0.25.

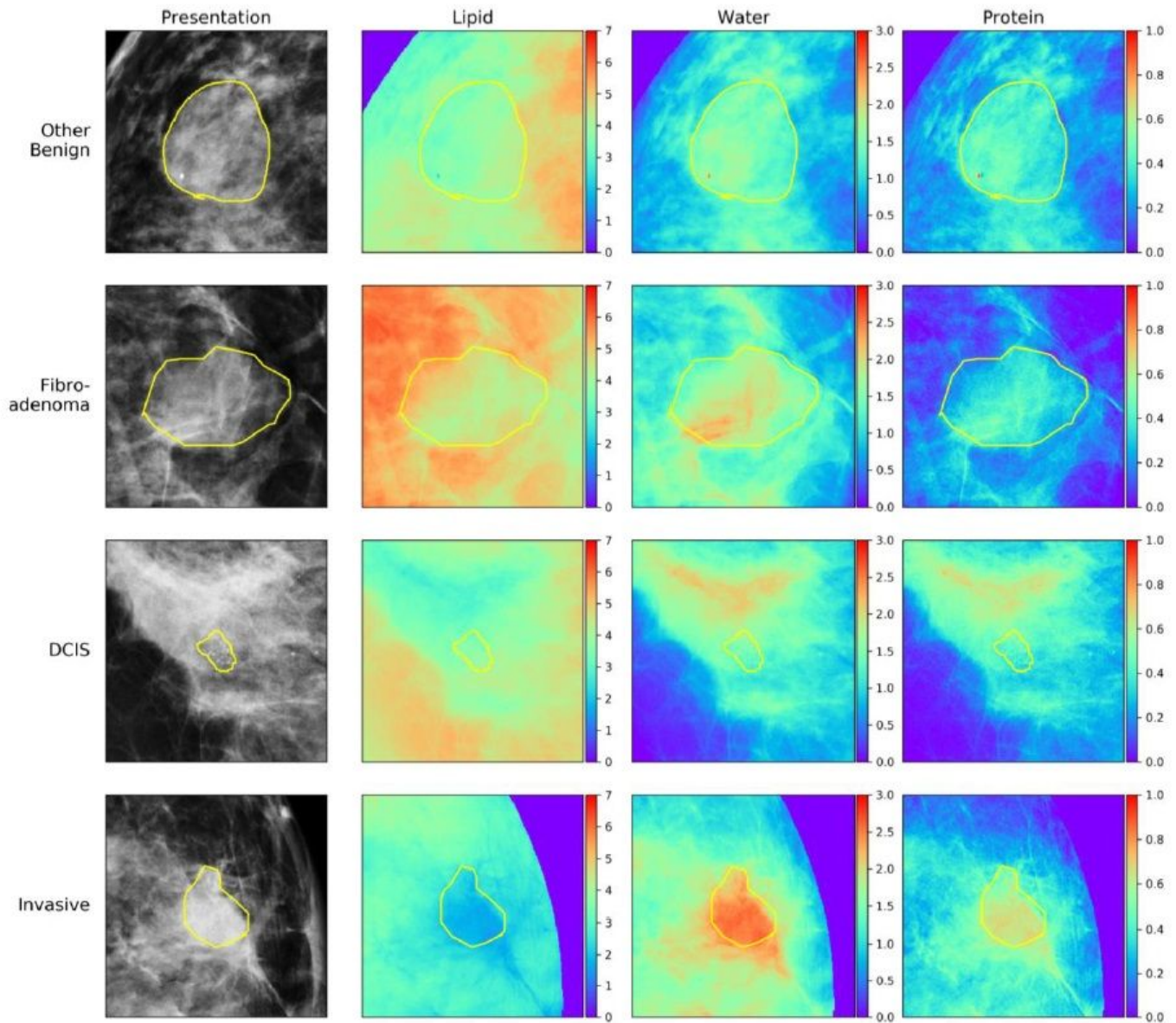


Figure 4

Compositional heatmaps of all lesion pathologies. Each row consists of a lesions with a different pathology. The first column contains the standard mammogram presentation, the second, third, and fourth columns contain the corresponding 3CB LWP thickness map. Colorbars adjacent to each 3CB map indicate thickness in cm where red indicates areas of high thickness and thickness decreases towards the color violet. Thickness ranges are normalized across each column. Yellow lines are radiologist delniations of where biopsies were taken from which lesion pathology was determined.

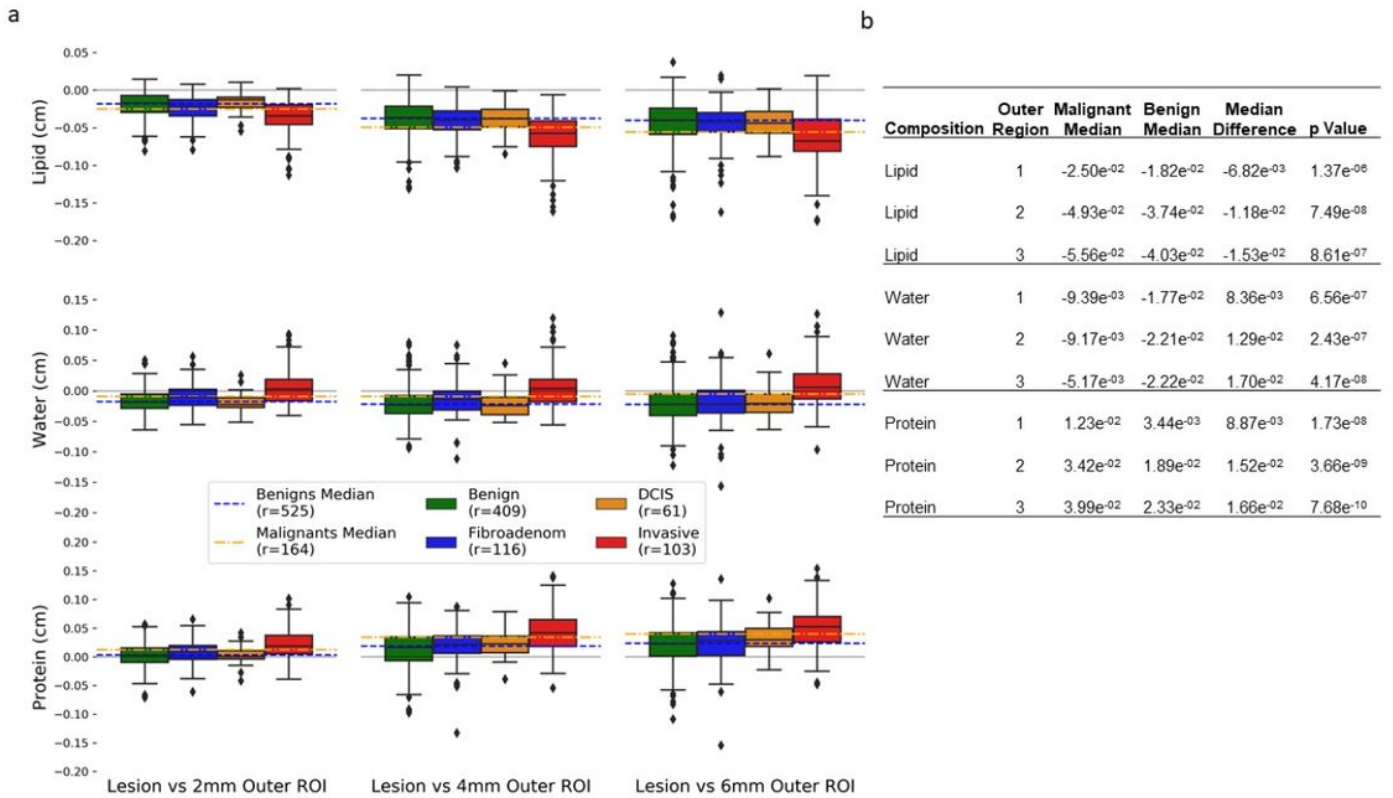


Figure 5

Lesion composition characterization. a, Differences between median composition values of the lesion and the outer regions were calculated for all radiologist ROIs. Column one, two, and three compares the composition within the lesion to the region 2mm, 4mm, and 6mm from its border respectively. Each row looks at a different compositional component, lipid, water, or protein. Calculated differences are stratified by the following lesion types; BN (green), FA (blue), DCIS (orange), and IDC (red). Median values of all benign lesions types, BN and FA, and malignant types, DCIS and IDC, are represented by blue and orange dashed lines respectively. Gray line indicates zero and ROIs that lay above this line have more of a given composition when compared to its corresponding background outer region. Boxes represent the 25 to 75% interquartile range and the center line represents the median. Whiskers represent 1.5 the interquartile range and outliers which fall outside that range are depicted as diamonds. b, Comparison between benign and malignant lesions compositions indicated by the space between blue and orange dashed lines in Figure 5a. are quantified in this table. P-values were calculated using a Welch's test for unequal variance and all p-values are significant indicating that benign and malignant lesions have uniquely different compositions as measured by 3CB.

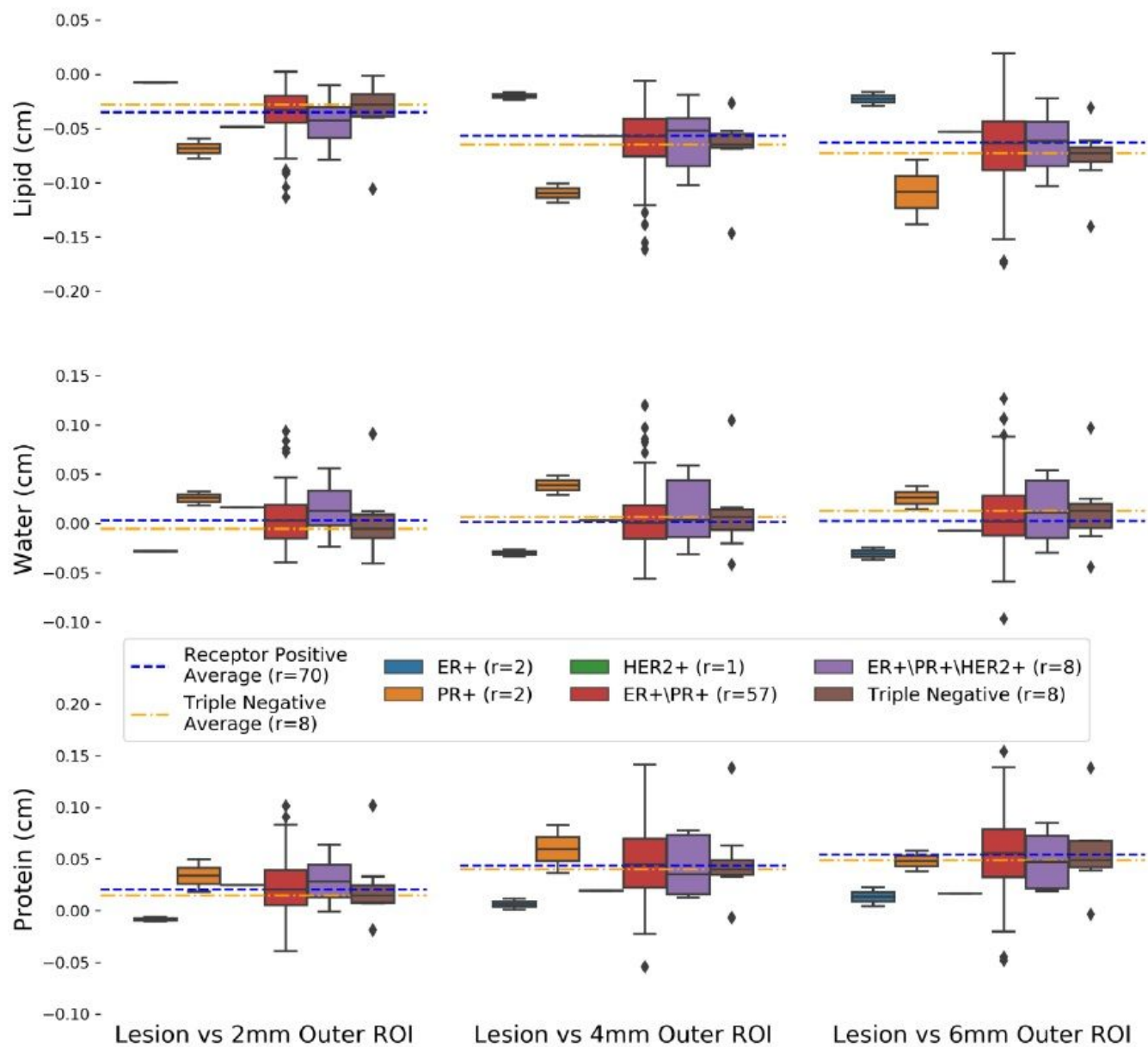


Figure 6

Hormone receptor composition characterization. Compositional difference between invasive lesions and their background are stratified by hormone receptor status. Median compositional difference between receptor positive and triple negative cancers are indicated by the blue and orange dashed lines respectively. Receptor positive median was calculated by including all lesion that contained either ER, PR, or HER2 receptor status.